Dalton Transactions

Accepted Manuscript

ROYAL SOCIETY OF CHEMISTRY

www.rsc.org/dalton

Table of contents

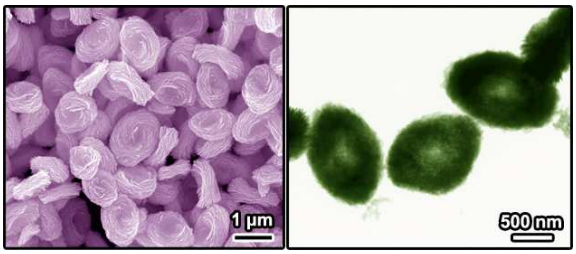

Doughnut-like, concave hierarchical structures of orthorhombic Sb_2WO_6 were firstly prepared and exhibited excellent visible-light-driven photocatalytic performance

Cite this: DOI: 10.1039/c0xx00000x

www.rsc.org/xxxxxx

ARTICLE TYPE

Solvothermal synthesis of orthorhombic Sb_2WO_6 hierarchical structures and their visible-light-driven photocatalytic activity

Sheng-Peng Hu [a, b], Cheng-Yan Xu [a, b, *], Fei-Xiang Ma [a, b], Lei Cao [a, b], Liang Zhen [a, b, *]

Received (in XXX, XXX) Xth XXXXXXXXX 20XX, Accepted Xth XXXXXXXXX 20XX

DOI: 10.1039/b000000x

We report the solvothermal synthesis of hierarchical structures of orthorhombic Sb_2WO_6 and their implementation as visible-light-driven photocatalyst for degradation of Rhodamine B. The obtained hierarchical structures constructed by tiny nanosheets are doughnut-like flat ellipsoids with concaves in the centres, and with typical sizes of 1.3 μm in length, 800 nm in width and 400 nm in thickness. The concave characteristics and sizes of Sb_2WO_6 hierarchical structures can be turned by adjusting the volume ratio of EG/H_2O. Time-dependent experiments reveal that the formation process of concave structures involves the aggregation of nanoparticles to form solid spheres, dissolution-recrystallization to form hierarchical structures subsequently, and Ostwald ripening process to shape the deserved concaves finally. Under visible-light irradiation, complete degradation of Rhodamine B is achieved within 180 min in the presence of Sb_2WO_6 hierarchical structures, which could be ascribed to the porous structures, high BET surface area (42.58 m^2 g^{-1}) and wide absorption in the visible-light region.

1. Introduction

Heterogeneous photocatalysis based on semiconductor oxides holds great potential for remedying environmental pollutions, and has received intense attention in recent decades[1-6]. As traditional photocatalysts, TiO_2 and ZnO have been widely applied in photocatalytic reactions. However, their intrinsic band gaps, making them only absorb the UV light, strongly limit their practical applications[7-11]. Therefore, the exploration of novel catalysts with visible light response is highly desirable for efficient light harvesting of solar energy. Two strategies have been developed to achieve the visible-light photocatalytic activity.[9, 12, 13]. One way is modification on the traditional catalysts. Taking the most important TiO_2 as an example[8, 14-17], several approaches have been proposed during the past few years: (1) doping of TiO_2. For example, N-doped TiO_2 nanobelts exhibit giant visible-light-response photocatalytic activity because the localized N 2*p* levels are above the top of valence band, and the 3*d* states of Ti^{3+} are below the conduction band[18]; (2) formation of heterostructures with narrow gap semiconductors[19], e.g. CeO_2[20], and In_2O_3[21], based on a novel capture-photodegradation-release mechanism; (3) decoration with noble metal nanoparticles including Au[22] and Ag[23], of which the plasmonic properties have been proved to enhance the photocatalysts activity of TiO_2 in visible light region; and (4) incorporation of carbonaceous nanomaterials such as graphene[24-26], and carbon nanotubes[27]. The other way is to develop novel semiconductors with suitable band gap with visible light response, such as Bi_2WO_6[28], $BiVO_4$[29], metal chalcogenides[30-35], and Ag_3PO_4[36, 37]. In addition, various methods have been developed to further improve their photocatalytic properties accordingly, including shape tuning[38, 39], doped with non-metal elements[40], and formation of semiconductors heterostructures[19, 41, 42] or graphene composites [43, 44].

Semiconductors with Aurivillius structure exhibit high electronic conductivity and appropriate band gap, and are thus considered as promising visible-light-driven photocatalysts [9, 45]. As an important member of Aurivillius family, Bi_2WO_6 has been extensively studied due to its intrinsic layer structures and related unique properties[28]. Sb_2WO_6 with Aurivillius structure can be also used as photocatalyst because of its similar crystal structure to that of Bi_2WO_6[46-48]. Bi_2WO_6 with various morphologies have been prepared in previous work[28, 38, 49]. In contrast, there are only a few reports concerning the synthesis of Sb_2WO_6 for photocatalysis applications. Very recently, triclinic Sb_2WO_6 hierarchical architectures were prepared by a hydrothermal method, and exhibited good photocatalytic activity for the reduction of azo compounds (MO degradation, 98 % after 140 min) under UV light irradiation[50]. Herein, we reported for the first time the preparation of orthorhombic Sb_2WO_6 hierarchical structures *via* a solvothermal method. The synergistic effect of EG and H_2O could tune the size and morphology of Sb_2WO_6 hierarchical structures. The formation mechanism was investigated based on time-dependent experiments. The photocatalytic activity of Sb_2WO_6 hierarchical structures was evaluated by the degradation of Rhodamine B (RhB) under visible light irradiation.

2. Experimental

2.1 Synthesis

All of the reagents were analytical grade and used without further

purification. In a typical synthesis procedure, 1 mmol $SbCl_3$ and 0.5 mmol Na_2WO_4•$2H_2O$ (2 : 1 in mole ratio) were dissolved into 10 mL ethylene glycol (EG) under magnetic stirring, respectively. The two solutions were mixed together in a 50 mL Teflon-lined autoclave, and then 10 mL distilled water was added into the above solution, followed by stirring for 30 min. The autoclave was maintained at 160 °C for 10 h, and then cooled to room temperature naturally. The obtained sample was denoted as S1. For comparison, other samples were prepared by adjusting the volume ratio of the EG/H_2O while keeping other parameters identical. The volume ratios of EG/H_2O are 2:1, 1:1, 1:2, 1:5, and the obtained samples were denoted as S1, S2, S3, S4, respectively. Another batch of sample using only H_2O as solvent was also prepared (sample S5).

2.2 Characterization

The phases of as-synthesized samples were identified by means of X-ray diffraction (XRD) with Rigaku D/max 2500 diffractometer using Cu K_α radiation (λ = 0.15418 nm). The morphologies and microstructures of the products were characterized by using a field-emission scanning electron microscope (FE-SEM, FEI Quanta 200F) and a transmission electron microscope (TEM, FEI Tecnai G^2 F30, 300 kV). Nitrogen adsorption-desorption isotherms were performed on a Micrometrics ASAP 2020 analyser at 77.35 K after degassing the sample at 100 °C for 2 h. The UV-vis diffuse reflectance spectrum of the samples was measured with UV-vis spectrometer (Shimadzu UV-2550), and $BaSO_4$ was used as reference. The photoluminescence spectrum was measured on a Hitachi F-4600 fluorescence spectrometer at room temperature. The excitation wavelength was 300 nm, and the emission slit was 5 nm.

2.3 Measurement of photocatalytic properties

The photocatalytic activities were evaluated by degradation of RhB in aqueous solution under visible light irradiation. In the experimental setup, a 300W xenon lamp (CEL-HXF 300, Beijing Au-light, China, I = 15 A) was employed as a light source and a 420 nm cut-off filter was used to provide only visible light irradiation (see Fig. S1, ESI). 100 mg of photocatalyst was added to 100 mL of RhB solution (c = 1×10^{-5} mol/L) and then magnetically stirred in dark for 60 min to reach adsorption-desorption equilibrium and uniform dispersibility. 3 mL aliquots were collected every 30 min and then centrifuged at the speed of 8000 r/min for 5 min to separate the catalysts from the RhB suspension. The degradation of RhB was evaluated by monitoring the characteristic absorbance peak centred at 554 nm using a Shimadzu UV-2550 UV-vis spectrometer.

3. Results and discussion

3.1 Characterization of Sb_2WO_6 hierarchical structures

Fig. 1 shows XRD pattern of the as-synthesized Sb_2WO_6 product prepared with EG/H_2O volume ratio of 2:1 (sample S1). All the diffraction peaks can be perfectly indexed to those of orthorhombic phase of Sb_2WO_6 with cell constants of a = 8.59 Å, b = 9.58 Å, and c = 6.12 Å (JCPDS card No. 50-1553). No other impurity peaks such as triclinic phase of Sb_2WO_6 or Sb_2O_3 are detected[50]. The broad diffraction peaks imply small grain sizes of the obtained sample.

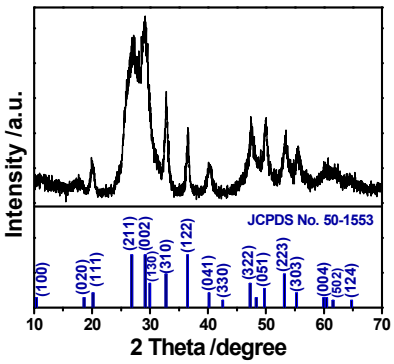

Fig. 1 XRD pattern of orthorhombic Sb_2WO_6 product prepared at 160 °C for 10 h with EG/H_2O volume ratio of 2:1 (sample S1). The lower panel shows the standard diffraction lines of orthorhombic Sb_2WO_6 (JCPDS No. 50-1553).

Fig. 2a-c gives FE-SEM images of sample S1. Low-magnification SEM images (Fig. 2a and b) depict that the product is composed of uniform doughnut-like flat ellipsoids with concaves in the centre, and the typical sizes are 1.3 μm in length, 800 nm in width and 400 nm in thickness. High-magnification SEM image (Fig. 2c) clearly reveals that the ellipsoids are assembled with numerous sheet-like structures with thicknesses of *ca.* 30 nm, implying the formation of hierarchical structures. The detailed morphologies and structure features were further investigated by TEM and high-resolution TEM (HRTEM), as shown in Fig. 2d-f. TEM image of the Sb_2WO_6 hierarchical structures confirms that the sizes of Sb_2WO_6 hierarchical structures are consistent with SEM observation. The clear contrast between the dark edges and the pale centre indicates the concave structures. Further close inspection (Fig. 2e) on the edge (marked with a rectangle in Fig. 2d) indicates that the hierarchical structure is constructed by nanosheets with mean width of 40 nm. HRTEM image (Fig. 2f) of the nanosheet showing the clear lattice fringes demonstrates that the nanosheet is crystallized. The interplanar lattice spacings are determined to be 0.307 and 0.295 nm, which are in good agreement with the interplanar spacings of (002) and (130) planes of orthorhombic Sb_2WO_6, respectively.

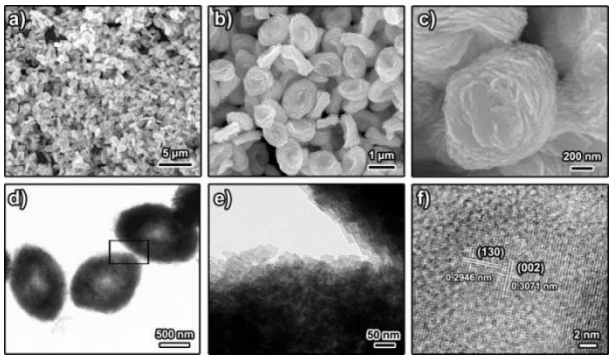

Fig. 2 FE-SEM (a-c), TEM (d, e) and HRTEM images (f) of Sb_2WO_6 hierarchical structures prepared at 160 °C for 10 h with EG/H_2O volume ratio of 2:1 (sample S1).

The specific surface area and porosity of sample S1 was measured by using N_2 adsorption-desorption isotherms. As shown in Fig. 3, the isotherm displays a type-IV isotherm with an apparent hysteresis loops (type H3) at relative pressure (P/P_0) range of 0.45 to 1.0, implying the presence of mesopores in

Sb_2WO_6 hierarchical structures[51, 52]. The mesopores are formed most likely due to the aggregation of nanosheets[53]. The BET surface area of the prepared Sb_2WO_6 hierarchical structures is determined to be 42.58 $m^2 g^{-1}$. These results are further confirmed by the corresponding pore-size distribution curves. As shown in the inset of Fig. 3, the pore-size distribution curve is quite broad (from 2 to 170 nm) with large mesopores centre at *ca.* 13 nm, and these pores can be attributed to the space between the intercrossed nanosheets. Such porous structures might be benefit for photocatalysis because they can provide efficient transport pathways to contaminant [54].

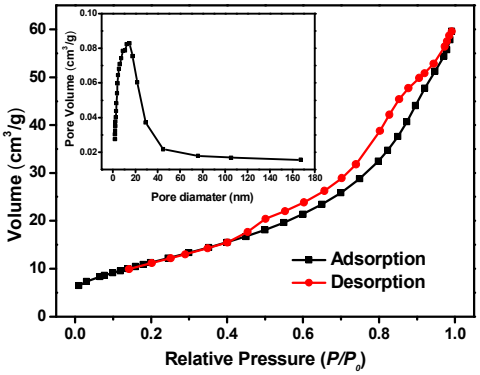

Fig. 3 N_2 adsorption-desorption isotherm curve of Sb_2WO_6 hierarchical structures (sample S1). Inset is the pore size distribution.

3.2 Effects of EG/H_2O volume ratio on morphology of Sb_2WO_6 hierarchical structures

EG has been used as solvent and soft template for the morphology tuning of various kinds of nanomaterials because of its unique physical and chemical properties[55, 56]. Due to the coordination habit with metal ions and viscosity change of the solution, EG can inhibit the hydrolysis of metal ions, decrease the reaction rate and serve as a soft template, and then yield products with uniform size[55, 57]. In contrast, the reaction with H_2O as solvent is fast, resulting enhanced growth rate, and thus uniform product is hard to be obtained. In this work, the effect of EG/H_2O volume ratio on the formation of Sb_2WO_6 hierarchical structures was investigated. Pure Sb_2WO_6 were obtained with different EG/H_2O volume ratios ranging from 1:1 to 1:5 as well as using only H_2O as solvent (see XRD pattern Fig. S2, ESI. The slight difference is reflected in the crystallinity, which will affect the photocatalytic activity. In contrast, the morphology of Sb_2WO_6 hierarchical structures highly depends on the EG/H_2O volume ratios, as shown in Figs. 4 and S3. With the decrease of EG volume fraction, the size of Sb_2WO_6 hierarchical structures becomes larger (detailed data are listed in Table 1), and the concave characteristics gradually diminish. TEM images of samples S2–S4 imply the absence of porous structure at high volume fraction of H_2O. When only H_2O was used as solvent, product with irregular shapes was obtained, and detailed morphologies were shown in Figs. S3 and S4, ESI.

It is believed that both Sb^{3+} and WO_4^{2-} can coordinate with EG to form the capping complex[58, 59]. The complex formation was further confirmed by the fact that no precipitate was obtained due to the high capping effect of EG when only EG was used as solvent. On the other hand, the presence of H_2O is essential in the solvent system for reducing the coordinating ability of EG molecules with M (Sb^{3+} and WO_4^{2-})[60]. Water molecules could break the complexes and lead to the hydrolysis of Sb^{3+}. The larger H_2O volume, the higher possibility of complex interruption[60, 61]. With the increasing volume fraction of water, the complex interruption probability increases, resulting in a rise of nucleation rate and aggregation, and then the size of individual hierarchical structure increases gradually. Interestingly, nanosheets are compactly aggregated from both ends to the middle of hierarchical structures, leading to the disappearance of concaves and the decline of specific surface area, as shown in Fig. 4 and Table 1. The reason may be the rapid nucleation and aggregation caused by increasing volume fraction of water. It is obvious that the synergistic effects of EG and H_2O play critical roles in the formation of Sb_2WO_6 hierarchical structures.

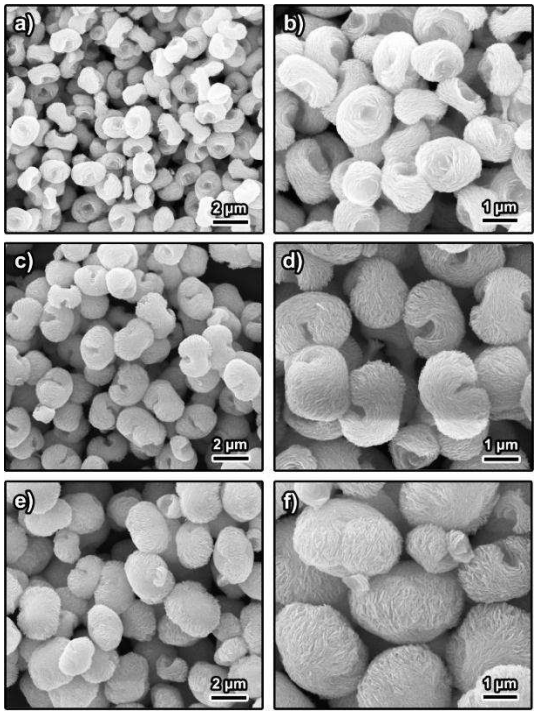

Fig. 4 SEM images of Sb_2WO_6 hierarchical structures prepared at 160 °C for 10 h with different volume ratios of EG/H_2O. (a, b) 1:1 (S2); (c, d) 1:2 (S3); (e, f) 1:5 (S4).

Table 1 Detailed sizes, specific surface areas and reaction constants of Sb_2WO_6 hierarchical structures prepared with different volume ratios of EG/H_2O.

Sample	Volume ratio of EG/H_2O	Morphology (length/width/thickness)	S_{BET} ($m^2 g^{-1}$)	k (min^{-1})
S1	2:1	1.3μm/800nm/400nm	42.58	0.01803
S2	1:1	1.8μm/1.5μm/680nm	34.72	0.00492
S3	1:2	2.6μm/2μm/800nm	20.4	0.00771
S4	1:5	3.4μm/2.6μm/1.2μm	19.37	0.00585
S5	H_2O	irregular shape	-	0.00729

3.3 Formation mechanism of Sb_2WO_6 hierarchical structures

Experiments with different reaction durations were carried out to explore the possible formation mechanism of Sb_2WO_6 hierarchical structures. Fig. 5 gives FE-SEM images of the

products obtained at different reaction durations, and the corresponding XRD patterns are displayed in Fig. 6. Amorphous nanoparticles were formed in the initial reaction stage with short reaction duration of 20 min, as shown in Fig. 5a and Fig. 6. After solvothermal treatment for 40 min, some aggregated microspheres along with particles with diameters of about 500 nm were formed (Fig. 5b). When the reaction was further prolonged to 1 h, hierarchical structures consisting of nanosheets were obtained, along with a few aggregated spheres (Fig. 5c). The corresponding TEM image indicated the solid structure of the aggregated spheres with reaction duration of 1 h (Fig. S5, ESI). As the reaction proceeded, hierarchical structures with irregular length from 800 nm to 2 μm were obtained after 4 h of reaction time (Fig. 5d). XRD pattern in Fig. 6 indicated the product crystallized after 1 h of reaction. Finally, uniform orthorhombic Sb_2WO_6 hierarchical structures with length of *ca.* 1.3 μm were obtained after 10 h reaction (Fig. 2).

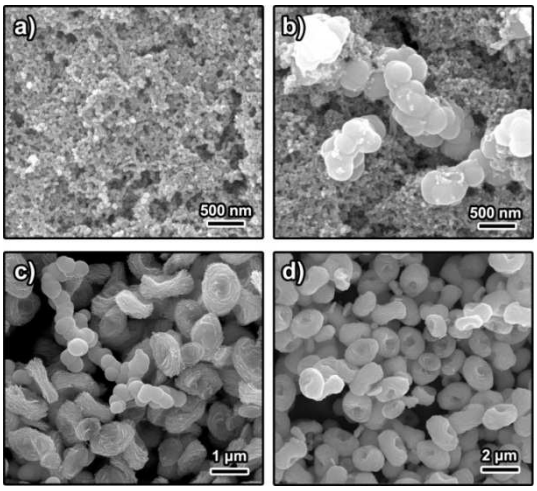

Fig. 5 Morphology evolution of the Sb_2WO_6 hierarchical structures at different reaction durations with EG/H_2O volume ratio of 2:1. (a) 20 min; (b) 40 min; (c) 1 h; (d) 4 h.

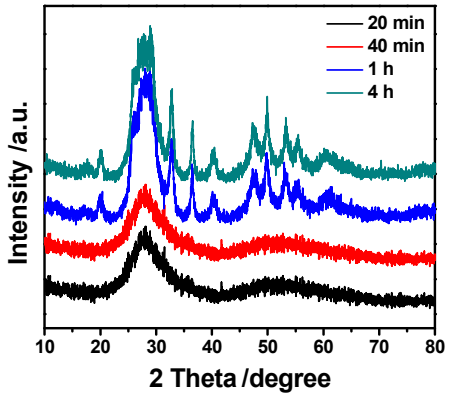

Fig. 6 XRD patterns of the products obtained at different reaction durations with EG/H_2O volume ratio of 2:1.

Based on the above data, the possible formation mechanism of Sb_2WO_6 hierarchical structures was put forward as follows. As shown in Scheme 1, $SbCl_3$ and Na_2WO_4•$2H_2O$ were completely dissolved into EG and formed stable complexes firstly (Sb^{3+}-EG and WO_4^{2-}-EG complexes), and no precipitation was observed because of the strong coordination between EG and metal ions. When H_2O was added into the solution quickly, green precipitation formed immediately because H_2O might reduce the total viscosity of solution and break the coordination of EG molecule with Sb^{3+} and WO_4^{2-} ions. At the initial stage of the solvothermal reaction, amorphous nanoparticles were formed firstly. The instability of reaction system led to the aggregation and subsequent growth of nanoparticles driven by the surface energy reduction, and then solid spheres agglomerates were formed with increasing solvothermal time (step 1 in Scheme 1).. These solid spheres were also unstable and wrapped by functional groups, which benefited the second nucleation on their surface. Meanwhile, because of the orthorhombic structure and intrinsic anisotropic growth habit of Sb_2WO_6[46, 50], the $Sb_2O_2^{2+}$ and WO_4^{2-} ions in the solution tended to nucleate and form nanosheets attached to the surface of solid spheres at the expense of other spheres dissolution. Then, a few hierarchical structures with solid centre were formed firstly, accompanying with the residual solid spheres (step 2 in Scheme 1)[52, 55]. With the prolonging of reaction time, the residual spheres were totally turned to hierarchical structures, and the internal part of the formed hierarchical structures gradually dissolved and recrystallized through Ostwald ripening process (step 3 in Scheme 1)[62, 63]. Finally, the hierarchical structures with concaves were obtained because of mass diffusion and Ostwald ripening (step 4 in Scheme 1). Thus, the formation mechanism may involve three steps: the aggregation of nanoparticles to form solid spheres, dissolution-recrystallization to form hierarchical structures and Ostwald ripening process to shape structures with the concave.

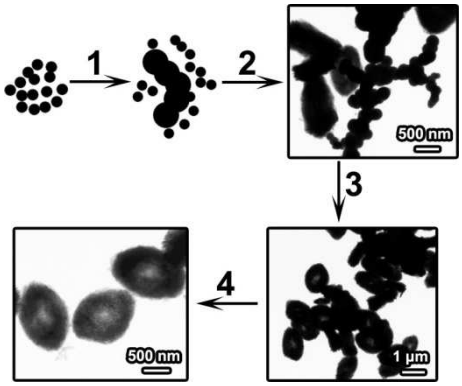

Scheme 1 The possible formation mechanism of Sb_2WO_6 hierarchical structures.

3.4 Photocatalytic properties of Sb_2WO_6 hierarchical structures

The optical absorptions of the obtained Sb_2WO_6 samples were measured by UV-vis diffuse reflectance spectrometer. As shown in Fig. 7, all the samples prepared with different volume ratios of EG/H_2O show strong absorption in the UV- and visible-light regions. The absorption edges of samples locate at around 550 nm which are red shifted compared with triclinic phase Sb_2WO_6 sample (500 nm) in previous work[50]. The red shift will benefit the visible light photocatalytic activities. The band gap can be roughly estimated by the formula, E_g (eV) = 1240 / λ (nm)[12], where λ is the absorption edges of semiconductors. The estimated band gap of orthorhombic Sb_2WO_6 hierarchical structures is about 2.25 eV.

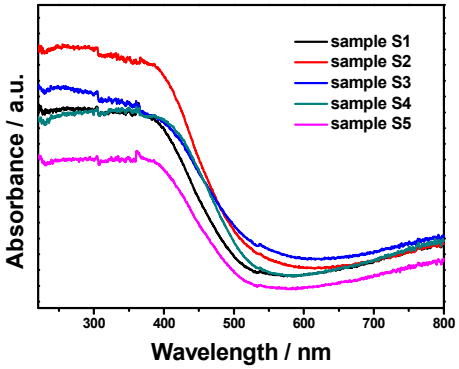

Fig. 7 UV-vis diffuse reflection spectra of Sb_2WO_6 hierarchical structures prepared at 160 °C for 10 h with different volume ratios of EG/H_2O.

The photocatalytic activity of Sb_2WO_6 hierarchical is evaluated using RhB as target dye under visible light irradiation (λ > 420 nm). The suspensions are firstly stirred in dark to reach the adsorption-desorption equilibrium (Fig. S6, ESI). Fig. 8a displays the adsorption spectra of RhB solution degraded by Sb_2WO_6 hierarchical structures obtained at EG/H_2O volume ratio of 2:1 (sample S1) under visible light irradiation. It can be found that the intensity of the absorption peak at 554 nm of RhB decrease with the increase of irradiation time, which was also verified by the colour change from the initial pink to colourless (Fig. S7, ESI). No new absorption bands are observed in both UV and visible regions[64]. The degradation rates of RhB by different samples are compared in Fig. 8b. RhB is stable in the absence of catalyst under visible light irradiation. Sample S1 exhibits highest photocatalytic activity at precondition of the deduction of the absorption fraction. It should be noted the adsorption of sample S5 is higher than other samples due to its irregular shape (Fig. S4, ESI), while its photocatalytic efficiency is lower.

The pseudo-first-order linear relationship is revealed by the plots of $ln(C_0/C)$ *vs.* irradiation time (t), shown in Fig. S8 (supplementary information), and the corresponding reaction constant k for different samples are summarized in Table 1. Compared with other samples with different morphologies, sample S1 possesses the best photocatalytic performance. The high photocatalytic activity of the sample S1 can be attributed to the unique structure of nanosheets on the surface of hierarchical structures, and plenty of meso- and macropores between nanosheets can provide more efficient transport paths for photocatalysis[61, 65, 66]. Moreover, the BET surface area of sample S1 is higher than that of other samples. High BET surface area and porous structure mean that the sample can provide more active reaction sites and help to promote the separation efficiency of the electron-hole pairs in photocatalytic reaction[67, 68]. The degradation efficiency of sample S2, S3 and S4 is lower than that of S1 due to their smaller BET surface area, solid structure, lower crystallinity, larger sizes of hierarchical structures and their slightly enclosed centres packaged by the outer nanosheets Photoluminescence (PL) emission spectrum is used to reveal the migration, transfer, and recombination processes of photogenerated electron–hole pairs in the semiconductors[69]. Fig. S9 shows the comparison of the PL emission spectra of all the samples. When the excitation wavelength is 300 nm, all the samples have broad but lower emission spectra, and the sample S1 shows the lowest intensity, indicating the lowest recombination of photogenerated charge carriers, which means the highest photocatalytic activity of sample S1. Moreover, the adsorption of sample S5 is higher than other samples due to its irregular shape (Fig. S4). Therefore, it is obvious that the Sb_2WO_6 hierarchical structures composed of nanosheets with a concave perform good photocatalytic property under visible light irradiation. The obtained Sb_2WO_6 hierarchical structures are used for 3 times to evaluate its stability. As shown in Fig. S10, the percentages of removal due to photocatalytic degradation during the cycling test are 83.2%, 83.0% and 80.7% for 1st, 2nd and 3rd run, respectively, depicting the good photo-stability of Sb_2WO_6 product. The corresponding XRD pattern and SEM images (Figs. S11 and S12) of the used catalyst indicate the chemical stability and durability of the catalyst. As orthorhombic Sb_2WO_6 nanomaterials are firstly used in photocatalysis, it is promising to explore methods for photocatalytic activities improvement[1, 10, 40, 70].

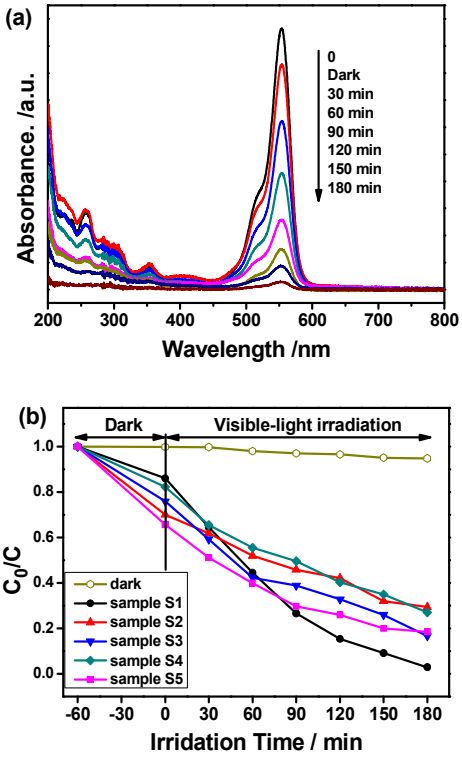

Fig. 8 (a) Temporal evolution of the absorption spectra of RhB solution in the presence of Sb_2WO_6 hierarchical structures (sample S1) under visible light irradiation; (b) photocatalytic degradation of RhB by different photocatalysts under visible light irradiation.

4. Conclusions

In summary, a facile solvothermal method was developed for the synthesis of orthorhombic Sb_2WO_6 hierarchical porous structures with building blocks of tiny nanosheets for the first time. The volume ratio of EG/H_2O could adjust the size and concave of hierarchical structures due to their synergistic effect, and reaction duration revealed that the formation of hierarchical structures might involve the following process: aggregation, dissolution-recrystallization and Ostwald ripening. The as-prepared orthorhombic Sb_2WO_6 hierarchical structures have good photocatalytic activity for RhB degradation under visible light

irradiation due to its unique morphology and high specific surface area.

Notes and references

[a] *School of Materials Science and Engineering, Harbin Institute of Technology, Harbin 150080, China. Fax: 86-451-8641-3922; Tel: 86-451-8641-2133; E-mail: cy_xu@hit.edu.cn; lzhen@hit.edu.cn.*
[b] *MOE Key Laboratory of Micro-system and Micro-structures Manufacturing, Harbin Institute of Technology, Harbin 150080, China*

† Electronic Supplementary Information (ESI) available: [Light spectrum of xenon lamp, additional XRD patterns, SEM and TEM images and PL spectra of Sb_2WO_6 products prepared at different conditions, dark experiments, digital photograph of degraded RhB solutions at different time intervals, linear fitting of $\ln(C_0/C)$ vs. reation time (t) over differerent photocatalysts, and cycling performance of sample S1.]. See DOI: 10.1039/ b000000x/

1. Y. Qu and X. Duan, *Chem. Soc. Rev.*, 2013, **42**, 2568-2580.
2. H. Kisch, *Angew. Chem., Int. Ed.*, 2013, **52**, 812-847.
3. S. Pasternak and Y. Paz, *ChemPhysChem.*, 2013, **14**, 2059-2070.
4. J. Tian, Y. Sang, G. Yu, H. Jiang, X. Mu and H. Liu, *Adv. Mater.*, 2013, **25**, 5075-5080.
5. Y. Wang, J. Lin, R. Zong, J. He and Y. Zhu, *J. Mol. Catal. A*, 2011, **349**, 13-19.
6. X. Lang, X. Chen and J. Zhao, *Chem. Soc. Rev.*, 2014, **43**, 473-486.
7. Z. Wang, X. Zhan, Y. Wang, S. Muhammad, Y. Huang and J. He, *Nanoscale*, 2012, **4**, 2678-2684.
8. H. Tong, S. Ouyang, Y. Bi, N. Umezawa, M. Oshikiri and J. Ye, *Adv. Mater.*, 2012, **24**, 229-251.
9. C. Chen, W. Ma and J. Zhao, *Chem. Soc. Rev.*, 2010, **39**, 4206-4219.
10. Y. Wang, Q. Wang, X. Zhan, F. Wang, M. Safdar and J. He, *Nanoscale*, 2013, **5**, 8326-8339.
11. G. Lui, J.-Y. Liao, A. Duan, Z. Zhang, M. Fowler and A. Yu, *J. Mater. Chem. A*, 2013, **1**, 12255-12262.
12. A. Kudo and Y. Miseki, *Chem. Soc. Rev.*, 2009, **38**, 253-278.
13. X. Hu, G. Li and J. C. Yu, *Langmuir*, 2010, **26**, 3031-3039.
14. D. V. Bavykin, J. M. Friedrich and F. C. Walsh, *Adv. Mater.*, 2006, **18**, 2807-2824.
15. A. Fujishima, X. Zhang and D. Tryk, *Surf. Sci. Rep.*, 2008, **63**, 515-582.
16. W. J. Ong, L. L. Tan, S. P. Chai, S. T. Yong and A. R. Mohamed, *Nanoscale*, 2014, 6, 1946-2008..
17. W. J. Ong, L. L. Tan, S. P. Chai, S. T. Yong and A. R. Mohamed, *ChemSusChem.*, 2014, **7**, 690-719.
18. J. Wang, D. N. Tafen, J. P. Lewis, Z. Hong, A. Manivannan, M. Zhi, M. Li and N. Wu, *J. Am. Chem. Soc.*, 2009, **131**, 12290-12297.
19. Y. Wang, F. Wang and J. He, *Nanoscale*, 2013, **5**, 11291-11297.
20. J. Tian, Y. Sang, Z. Zhao, W. Zhou, D. Wang, X. Kang, H. Liu, J. Wang, S. Chen, H. Cai and H. Huang, *Small*, 2013, **9**, 3864-3872.
21. J. Mu, B. Chen, M. Zhang, Z. Guo, P. Zhang, Z. Zhang, Y. Sun, C. Shao and Y. Liu, *ACS Appl. Mater. Interfaces*, 2012, **4**, 424-430.
22. Q. Zhang, D. Q. Lima, I. Lee, F. Zaera, M. Chi and Y. Yin, *Angew. Chem., Int. Ed.*, 2011, **50**, 7088-7092.
23. K. Awazu, M. Fujimaki, C. Rockstuhl, J. Tominaga, H. Murakami, Y. Ohki, N. Yoshida and T. Watanabe, *J. Am. Chem. Soc.*, 2008, **130**, 1676-1680.
24. Y. H. Hu, H. Wang and B. Hu, *ChemSusChem*, 2010, **3**, 782-796.
25. Q. Xiang, J. Yu and M. Jaroniec, *Nanoscale*, 2011, **3**, 3670-3678.
26. L. Liu, Z. Liu, A. Liu, X. Gu, C. Ge, F. Gao and L. Dong, *ChemSusChem*, 2014, **2**, 618–626.
27. W.-J. Ong, M. M. Gui, S.-P. Chai and A. R. Mohamed, *RSC Adv.*, 2013, **3**, 4505-4509.
28. L. Zhang, H. Wang, Z. Chen, P. K. Wong and J. Liu, *Appl. Catal., B*, 2011, **106**, 1-13.
29. Y. Park, K. J. McDonald and K. S. Choi, *Chem. Soc. Rev.*, 2013, **42**, 2321-2337.
30. Z. Mei, S. Ouyang, D. M. Tang, T. Kako, D. Golberg and J. Ye, *Dalton Trans.*, 2013, **42**, 2687-2690.
31. X. An, J. C. Yu, F. Wang, C. Li and Y. Li, *Appl. Catal., B*, 2013, **129**, 80-88.
32. M. R. Gao, Y. F. Xu, J. Jiang and S. H. Yu, *Chem. Soc. Rev.*, 2013, **42**, 2986-3017.
33. Z. Wu, L. Chen, C. Xing, D. Jiang, J. Xie and M. Chen, *Dalton Trans.*, 2013, **42**, 12980-12988.
34. Z. Wang, H. Yin, C. Jiang, M. Safdar and J. He, *Appl. Phys. Lett.*, 2012, **101**, 253109-256101.
35. Z. Wang, X. Zhan, Y. Wang, M. Safdar, M. Niu, J. Zhang, Y. Huang and J. He, *Appl. Phys. Lett.*, 2012, **101**, 073105.
36. Y. Bi, S. Ouyang, N. Umezawa, J. Cao and J. Ye, *J. Am. Chem. Soc.*, 2011, **133**, 6490-6492.
37. W. F. Yao, B. Zhang, C. P. Huang, C. Ma, X. L. Song and Q. J. Xu, *J. Mater. Chem.*, 2012, **22**, 4050-4055.
38. L. Zhang and Y. Zhu, *Catal. Sci. Technol.*, 2012, **2**, 694-706.
39. M. Liu, L. Piao, W. Lu, S. Ju, L. Zhao, C. Zhou, H. Li and W. Wang, *Nanoscale*, 2010, **2**, 1115-1117.
40. C. Yin, S. Zhu, Z. Chen, W. Zhang, J. Gu and D. Zhang, *J. Mater. Chem. A*, 2013, **1**, 8367-8378.
41. Y. Wang, X. Bai, C. Pan, J. He and Y. Zhu, *J. Mater. Chem.*, 2012, **22**, 11568-11573.
42. F. Wang, Y. Wang, X. Zhan, M. Safdar, J. R. Gong and J. He, *CrystEngComm*, 2013, 16, 1389-1394..
43. W. Tu, Y. Zhou and Z. Zou, *Adv. Funct. Mater.*, 2013, **23**, 4996-5008.
44. R. K. Upadhyay, N. Soin and S. S. Roy, *RSC Adv.*, 2014, **4**, 3823-3852.
45. H. Zhou, Y. Qu, T. Zeid and X. Duan, *Energ. Environ. Sci.*, 2012, **5**, 6732-6743.
46. C. Zhang and Y. Zhu, *Chem. Mater.*, 2005, **17**, 3537-3545.
47. A. Martínez-de la Cruz and F. E. Longoria Rodríguez, *Mater. Res. Bull.*, 2007, **42**, 1851-1855.
48. A. Castro, P. Millan and R. Enjalbert, *Mater. Res. Bull.*, 1995, **30**, 871-882.
49. Y. Huang, J. Wu, M. Huang, J. Lin and Y. Huang, *Sci. China Chem.*, 2011, **54**, 211-216.
50. J. Bi, Y. Liu, S. Liang, W. Wu, R. Yuan and L. Wu, *J. Nanopart. Res.*, 2013, **15**, 1661-1670.
51. J. Lee, J. Kim and T. Hyeon, *Adv. Mater.*, 2006, **18**, 2073-2094.
52. L. Xu, X. Yang, Z. Zhai and W. Hou, *CrystEngComm*, 2011, **13**, 7267-7275.
53. F. Dong, W.-K. Ho, S. C. Lee, Z. Wu, M. Fu, S. Zou and Y. Huang, *J. Mater. Chem.*, 2011, **21**, 12428-12436.
54. Q. Xiang, B. Cheng and J. Yu, *Appl. Catal., B*, 2013, **138-139**, 299-303.

55. Y.-X. Zhou, H.-B. Yao, Q. Zhang, J.-Y. Gong, S.-J. Liu and S.-H. Yu, *Inorg. Chem.*, 2009, **48**, 1082-1090.
56. H. Yue, Y. Zhao, X. Ma and J. Gong, *Chem. Soc. Rev.*, 2012, **41**, 4218-4244.
57. H. Du, L. Jiao, Q. Wang, Q. Huan, L. Guo, Y. Si, Y. Wang and H. Yuan, *CrystEngComm*, 2013, **15**, 6101-6105.
58. G. Tian, Y. Chen, W. Zhou, K. Pan, Y. Dong, C. Tian and H. Fu, *J. Mater. Chem.*, 2011, **21**, 887-891.
59. M. Shang, W. Wang and H. Xu, *Cryst. Growth Des.*, 2008, **9**, 991-996.
60. T. Ghoshal, S. Kar and S. Chaudhuri, *Cryst. Growth Des.*, 2006, **7**, 136-141.
61. D. He, L. Wang, H. Li, T. Yan, D. Wang and T. Xie, *CrystEngComm*, 2011, **13**, 4053-4059.
62. W. Shi, S. Song and H. Zhang, *Chem. Soc. Rev.*, 2013, **42**, 5714-5743.
63. X. W. Lou, L. A. Archer and Z. Yang, *Adv. Mater.*, 2008, **20**, 3987-4019.
64. H. Fu, C. Pan, W. Yao and Y. Zhu, *J. Phys. Chem. B*, 2005, **109**, 22432-22439.
65. Z.-Q. Li, X.-T. Chen and Z.-L. Xue, *CrystEngComm*, 2013, **15**, 498-502.
66. P. Madhusudan, J. Zhang, B. Cheng and G. Liu, *CrystEngComm*, 2013, **15**, 231-236.
67. X. Wang, J. C. Yu, C. Ho, Y. Hou and X. Fu, *Langmuir*, 2005, **21**, 2552-2559.
68. Y. Huo, J. Zhang, M. Miao and Y. Jin, *Appl. Catal., B*, 2012, **111-112**, 334-341.
69. G. Fu, G. Xu, S. Chen, L. Lei and M. Zhang, *Catal. Commun.*, 2013, **40**, 120-124.
70. J. Guo, S. Ouyang, H. Zhou, T. Kako and J. Ye, *J. Phys. Chem. C*, 2013, **117**, 17716-17724.